ARGONNE NATIONAL LABORATORY
9700 South Cass Avenue
Argonne, Illinois 60439

ANL-03/26

ADVANCED SENSORS FOR REAL-TIME CONTROL OF ADVANCED NATURAL-GAS RECIPROCATING ENGINE COMBUSTION

by

S. H. Sheen, H. T. Chien, and A. C. Raptis

Sensors, Instrumentation, & Nondestructive Evaluation (SI&NDE) Section
Energy Technology Division

October 2003

Work Sponsored by

U.S. DEPARTMENT OF ENERGY
Office of Power Technology

Argonne National Laboratory, a U.S. Department of Energy Office of Science laboratory, is operated by The University of Chicago under contract W-31-109-Eng-38.

Available electronically at http://www.doe.gov/bridge

Available for a processing fee to U.S. Department of Energy and its contractors, in paper, from:

U.S. Department of Energy
Office of Scientific and Technical Information
P.O. Box 62
Oak Ridge, TN 37831-0062
phone: (865) 576-8401
fax: (865) 576-5728
email: reports@adonis.osti.gov

CONTENTS

FIGURES

TABLES

ACKNOWLEDGMENTS

This program was supported by the U.S. Department of Energy (DOE), Office of Power Technology. We thank Mr. J. A. Mavec, DOE program manager, for his continuous interest in and support of this project, and Mr. J. A. Jendrzejczyk for his contribution to this work. Laboratory work performed by Mr. Howard Wei, summer student, is appreciated.

ABSTRACT

This is the final report of a three-year project under a Department of Energy Advanced Reciprocating Engine Systems contract. The goal of this project is to develop advanced sensors for real-time combustion monitoring of advanced natural-gas reciprocating engines. Two sensor technologies, ion-mobility spectrometry (IMS) and acoustic gas sensing, were tested for detection of NO_x emissions and monitoring of natural-gas composition. This project examined two novel approaches: use of a corona/spark-discharge ionization source for IMS, and acoustic-relaxation spectra of natural gas for the acoustic gas sensor. We have completed evaluation of laboratory prototypes of both sensors. In this report, we will describe the basic elements of the sensors, their operating and detection principles, their performance, and other issues. Design modifications and suggested applications of field prototypes will also be presented.

1.0 INTRODUCTION

This is the final report of Argonne National Laboratory's (ANL's) Advanced Reciprocating Engine Systems (ARES) project on the development of advanced sensors for real-time combustion monitoring of advanced natural-gas reciprocating engines. The project is funded by the Department of Energy (DOE), Office of Power Technology. The proposed development includes sensors to measure NO_x emissions and natural-gas composition. Both sensors are needed to optimize engine combustion and reduce NO_x emissions. Optimization can generally be achieved by adjusting the natural-gas/air ratio to control NO_x emissions.

The project originally proposed four tasks: (a) develop an ion-mobility spectrometry (IMS) NO_x emission sensor, (b) develop an acoustic natural-gas sensor, (c) develop a real-time combustion control system, and (d) field test sensors and control systems. To date, only tasks a and b have been accomplished; results are presented and discussed in this report. Section 2 of this report describes the IMS sensor and Section 3, the acoustic natural-gas sensor. In section 4, we provide our technical assessment of both sensors and suggest future development that will lead to field prototypes.

2.0 ION-MOBILITY SPECTROMETRY SENSOR

In this section, we present the basic sensor design, operating principle, and results of laboratory tests to determine the capability of the IMS sensor to detect NO_x. We also briefly describe other NO_x sensor technologies, their performance, and suggested applications.

The exhaust of a typical ARES engine is composed of 490 ppm methane (CH_4), 10 ppm ethane (C_2H_6), 200 ppm nitric oxide (NO), 300 ppm carbon monoxide (CO), 150 ppm hydrogen (H_2), 5% carbon dioxide (CO_2), and 10% water and nitrogen. Therefore, the NO_x sensor for ARES engine exhaust must consider potential cross sensitivity due to the presence of reducing gases such as CO and H_2 and potential interference from other gases, especially water.

2.1 Background

Nitric oxide and CO are the primary emissions of concern from combustion engines. In air and under sunlight, they interact with oxygen to form NO_2 and O_3, which are the major air pollutants released into the environment. Under the clean-air act, both emissions must be maintained at a very low level. Therefore, in-line sensors are needed to measure the emissions and provide feedback control of either the fuel/air ratio or the NO_x reduction process. A NO_x sensor has been the most active research topic in sensor technology. The ideal NO_x sensor that will ultimately be used by ARES or the automotive industry must be low cost, high sensitivity (ppm), sustainable in a harsh environment (high temperature, >500°C, flow rate, and humidity), and reliable.

To date, monitoring and detection of gas species are mainly achieved with semiconductor sensors. Commonly used semiconductor materials are oxides of metals such as zirconium (ZrO_2), [1] tungsten (WO_3), [2] and tin (SnO_2) [3]. These sensors have been applied primarily to the detection of oxygen, and their principles of operation rely on measuring either resistance change (SnO_2), conductance (WO_3), or current/voltage change (ZrO_2) across the semiconductor. Applications of these sensors to NO_x measurement have been examined. Both WO_3 and SnO_2 sensors show good sensitivity to NO_x at relatively low temperatures (200–300°C) when compared with ZrO_2 sensors that operate at a temperature above 500°C. In general, typical problems of metal oxide sensors are poor sensitivity, nonlinear response, long-term drift, and slow response/recovery time. To improve sensitivity and selectivity, dopants are often introduced [4,5]. Array sensor design [3,6] has also been investigated for reducing cross sensitivity problems.

Other metal oxide thin films under investigation for NO_x sensing [7], similar to sensors that use conducting organic thin films [8] and carbon nanotubes [9], are still in the early stage of development. Today, the most versatile semiconductor sensor for detecting NO_x emission is perhaps the ZrO_2–based sensor. An oxygen-detecting yttria-stabilized zirconia (YSZ) sensor is basically a potentiometric Nernst cell for oxygen detection that operates at an elevated temperature and measures the voltage across two electrodes. The measured voltage is directly related to the partial pressure of oxygen. The cell can also be operated as an electrochemical oxygen pump by applying a voltage across the cell electrodes. Because of these two operations, a YSZ cell can be modified to become a NO_x sensor. One of the modified sensor designs consists of a single closed-end YSZ tube. Two materials, a spinel-type oxide [10] and platinum, are used for the sensing and reference electrodes, respectively. Use of $CdCr_2O_4$ as the sensing electrode showed a lower detection limit of ≈20 ppm for NO_2 and 30 ppm for NO at 500 and 550°C, respectively. The cross sensitivities of this sensor to H_2, CO, CH_4, and CO_2 are small but the cross sensitivities between NO and NO_2 are significant. Therefore, various strategies for measuring total NO_x have been suggested [11]. In all, YSZ-based sensors for measuring NO_x show some promising characteristics but they still suffer from low operating temperature (500 vs. 700°C), slow response time, and long-term drift.

The ion-mobility spectrometer has been demonstrated to be a low-cost and fast-response gas sensor [12] that can be used in high-pressure and high-temperature environments. It measures the drift velocities of molecular ions, positive or negative, in a drift tube. The drift velocity depends on the size of the ion and the type of buffer gas present in the drift tube. In principle, if all of the interactions that occur between ions and molecules in the drift tube were known, the ion-mobility spectrum would be the fingerprint of the ion being measured. The drift time could be used for ion speciation and the peak amplitude could quantify the ions. However, in practice, ions often form clusters that complicate the IMS spectrum. Furthermore, the IMS spectrum also depends on buffer-gas composition, pressure, temperature, and flow rate. Therefore, the IMS spectrum may be difficult to interpret and may require calibration data for its application in identifying ions.

In an earlier project, we developed an IMS sensor for detecting hydrocarbons (HCs) [13]. The prototype IMS, which uses a ^{63}Ni β source, was built and tested. Positive ions of various HCs were measured. Results showed that the sensitivity of the IMS sensor was adequate to detect most HCs; however, significant interference from water vapor and poor reproducibility were observed. The IMS was also used to detect NO_x by operating it in a negative-ion mode. Results obtained with the radioactive ion source showed that the sensitivity of the IMS in detecting both NO and NO_2 was high, and both the drift time and amplitude were functions of NO_x concentration [14].

Under this project, we focused on developing a practical NO_x sensor based on the IMS technique. The targeted sensor must use a nonradioactive ionization source and operate under ambient conditions. A corona/spark discharge ionization source with a simple needle-metal-cylinder geometry was investigated. Preliminary results show that better sensitivity is obtained in spark-discharge than in corona-discharge mode of operation, and the primary negative ion detected is the negative NO_2 ion. The results were summarized in an earlier technical report [15] in which we identified several technical issues that must be examined before the IMS sensor can be used in the natural-gas engine exhaust environment. These issues include effects due to water vapor, drift time ambiguity, and complexity of the ion-molecule chemistry due to variations of the exhaust-gas composition. This report addresses primarily these issues.

2.2 IMS Design and Operating Principles

Figure 1 shows the basic design of the laboratory prototype IMS sensor. It consists of the corona discharge ionization source, a drift tube, and an ion detector. A shutter grid placed between the ionization source and the drift tube functions as the ion extractor. Gas is introduced directly into the ionization source and the ambient air or carrier gas is used as the buffer gas for most tests. Ions are formed through either direct electron bombardment or reactions between ions and molecules inside the ionization source. Product ions are then extracted into the drift tube and move down the tube to the detector in a uniform electric field. The ion drift velocity, a measurable quantity of IMS, is influenced by the applied electrical field (E) and the ion

concentration gradient $(\partial n/\partial x)$ [12]. To include only the linear terms, the drift velocity is given by

$$V = KE - \frac{D}{n}\left(\frac{\partial n}{\partial x}\right), \tag{1}$$

where n is ion concentration, D the diffusion coefficient, and K the ion mobility. The diffusion term is generally very small, especially under ambient conditions. Thus, the ion drift velocity provides a direct measure of ion mobility. The mobility of an ion in the drift tube is determined by the ion-neutral collisions. Based on classical mechanics, the ion mobility can be given as

$$K = \left(\frac{q}{n}\right)^{1/2}\left(\frac{1}{3\mu T_{eff}}\right)^{1/2}\left[\frac{1}{\Omega(T_{eff})}\right], \tag{2}$$

where μ is the reduced mass of ion and buffer gas, $T_{eff} = T + MV^2/3k$ (M is molecular weight of the buffer gas), and $\Omega(T_{eff})$ is the total scattering cross section (= πd^2, where d is the sum of the radii of the ion and the neutral molecule). Conceptually, different ions have different mobilities in the same medium. But, just as mass spectrometry determines the charge/mass ratio, the ion mobility determines the quantity of $q/\mu^{1/2}\Omega$. As the mass of the ion becomes much larger than the mass of the drift gas molecules, the measured mobility will be independent of the ion mass but totally controlled by the average collisional cross section of the ion and the drift gas. On the other hand, for a series of atomic ions in the same neutral gas, Ω is nearly constant, and the mobility is determined by the reduced mass, assuming q is fixed. In the case when the neutral buffer gas is a gas mixture, the mobility of an ion can be approximated by Blanc's law [16], given as

$$\frac{1}{K} = \sum_j \frac{X_j}{K_j}, \tag{3}$$

where X_J represents the mole fraction of the jth gas.

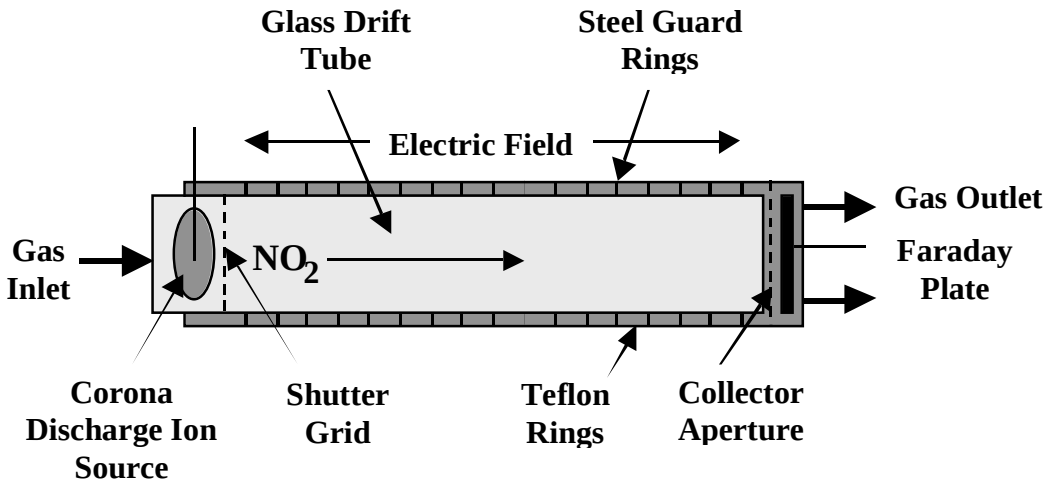

Figure 1. Basic design of ion-mobility spectrometer.

2.3 Laboratory Prototype Tests

Figure 2 shows a photograph of the laboratory prototype. It consists of (from left to right) a corona/spark discharge ionization source, an ion drift tube, and a Faraday plate. The geometry of the ionization source assembly is that of a needle/steel-cylinder. The drift tube is a glass tube, 0.625 inches in diameter and 2.5 inches long. The glass tube is embraced by a series of steel guard rings separated by Teflon rings and resistors. This arrangement establishes a uniform electrical field that accelerates the ions. To detect NO_x, the IMS is operated in the negative-ion mode. The steel cylinder is biased with a negative voltage so that negative ions are confined in the ionization cell until the shutter grid opens. Ion signals are detected by the Faraday plate, amplified by a low-noise, low-current preamplifier (Stanford Research Systems SR570) and processed by a 16-bit, 100 kS/s digitizer (National Instrument AT-MIO-16E-10). Typically, 100 averages were used for each ion spectrum of 80 ms scan time, which provided a total sensor response time of eight seconds. Table 1 lists the specific design parameters and typical operating conditions of the IMS sensor.

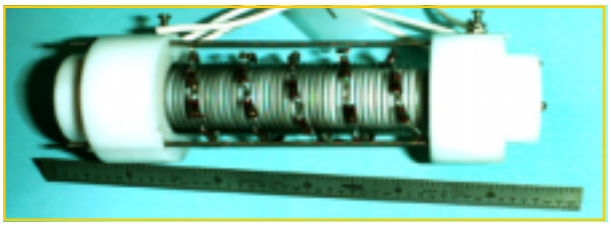

Figure 2. Photograph of laboratory prototype IMS sensor.

Table 1. Design parameters and operating conditions of IMS sensor.

Ion source		Shutter grid			Drift-tube electrical field	Detection Electronics		Pressure and Temperature
Needle-surface gap	Applied voltage	Pulse width	Pulse voltage	Frequency		Filter	Sensitivity	
0.25 cm	-3.0/-4.0kV	2 ms	140 V	12.5 Hz	220V/cm	3 kHz (LP)	2 nA/V	ambient

Laboratory tests designed to evaluate the prototype performance cover mainly the negative corona/spark discharge mode of operation. The negative high voltage to the discharge needle was supplied by a Bertan Associates power supply (series 225), which also measures the current from the needle to the cylindrical shell. Resistors with a total resistance of 2 MΩ were inserted between the power supply and the needle to limit the current to the needle. Test and carrier gases were acquired from AGA Specialty Gas. Gases used in this work are

Test gases: 483 ppm NO_2 in dry nitrogen
509 ppm nitric oxide, 515 ppm NO_x and dry nitrogen
Carrier gases: Dry nitrogen (99.9%)
Helium (99.99%)
Argon (99.99%)
Simulated exhaust gas (23.6 ppm SO_2, 121.2 ppm H_2, 398 ppm CO, 8.1% O_2, 10% CO_2, and N_2 the balance).

2.4 Results and Discussion

Use of a corona discharge ionization source for IMS has been the main interest in recent IMS development [17,18]. Aside from radioactive-material safety issues, the corona discharge ionization source provides better signal-to-noise ratio than the ^{63}Ni source. Furthermore, it may be easier to integrate the corona source into the design of a miniature IMS. However, the ionization chemistry is believed to be more complex for the corona discharge than the ^{63}Ni source. It has also been reported [18] that, because of the formation of NO_2^-, which quenches the formation of other product ions, the corona discharge ionization source is not a replacement for the ^{63}Ni source in the negative mode of IMS. Inasmuch as our interest is in the detection of NO_x, IMS with a negative-mode corona discharge ionization source may be ideal. Based on ion-molecule chemistry, the basic energy requirement for forming a negative molecular ion is determined by the electron affinity (EA) of the molecule. The EAs for the negative NO and NO_2 ions are ≈0.02 and 3.91 eV, respectively [12]. Therefore, the electron-impact ionization process is likely to produce both negative NO and NO_2 ions, but the NO_2 ions are thermodynamically more stable. Furthermore, in a plasma, a neutral NO molecule may be oxidized to NO_2, especially, in the presence of hydrocarbons [19,20]. It is, therefore, possible to estimate the total NO_x emissions by simply measuring NO_2 concentrations.

In general, the IMS sensor operates under vacuum and at elevated temperature [21], typically a few hundreds of torr in pressure in the drift tube and 100-200°C. Both pressure and temperature affect the IMS spectrum. At low temperature and high pressure, such as the ambient conditions, the IMS peaks are either very broad or move as the concentration in the drift tube changes. However, providing for vacuum and heating arrangements will further complicate the IMS sensor design. The tradeoff by operating in ambient conditions will be poor resolution and stability. In this report, we summarize test results obtained with a simple and practical IMS sensor operating under ambient conditions.

2.4.1 Corona/Spark Discharge Ionization Source

The ionization cell adopts basically a needle-shell design. The needle is insulated from the shell with a plastic tube and the tip of the needle faces the shell surface. In effect, the discharge arrangement is of needle-plane geometry. The gap between the needle and the shell plane was ≈0.25 cm. Figure 3 shows the current through the needle as a function of applied negative voltage for ambient air and 100 cm^3/min dry nitrogen flow. In ambient air, the discharge remained in corona discharge mode. But, with dry nitrogen flow, it turned into spark discharge even at –3.0 kV. The spark arc was clearly visible under daylight. The color of the arc varied with the flow composition; specifically, when the flow contained moisture, the color shifted to red. We found that spark discharge occurred when current suddenly jumped >0.5 mA. In both corona and spark discharges, a peak was detected when a NO_x/carrier gas mixture was introduced.

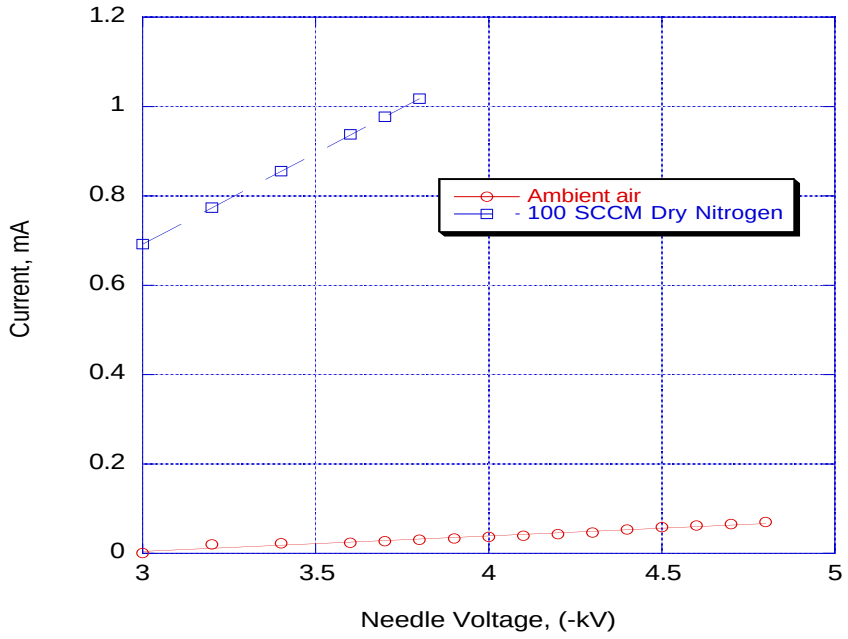

Figure 3. Current vs. voltage of corona ionization source for two gases.

Figure 4 shows the IMS spectra obtained under corona and spark discharges for simulated exhaust gas. The spectra clearly show that spark discharge (0.8 mA of current) produces a sharper peak than corona discharge (0.1 mA of current), and there is a significant drift time difference between the two peaks. The difference in drift time generally indicates that different negative ions are produced by the two discharge modes. However, in Fig. 4, we also show a spectrum of ambient air under corona discharge. This spectrum shows a peak at a drift time close to the simulated exhaust-gas peak produced under the same mode. The phenomenon implies that negative ions are produced by differing mechanisms: direct electron bombardment to produce O_2^- or O_3^- under the spark discharge mode and surface ionization to form the negative ions, which may contain heavy molecules evaporating from the needle surface under the corona discharge mode. Therefore, development of a negative-ion peak may strongly depend on the surface conditions and temperature of the needle and the metal shell. Even under spark discharge mode, we found that it took several minutes after the ion source was turned on for the negative-ion peak to reach an equilibrium drift time. Figure 5 shows the peak evolution, a trend from high to low drift time, indicating gradual reduction in ion size. In general, we have found that the spark discharge mode of operation gives a better signal-to-noise ratio than the corona discharge mode. Thus, we present mostly spark-discharge results in this report.

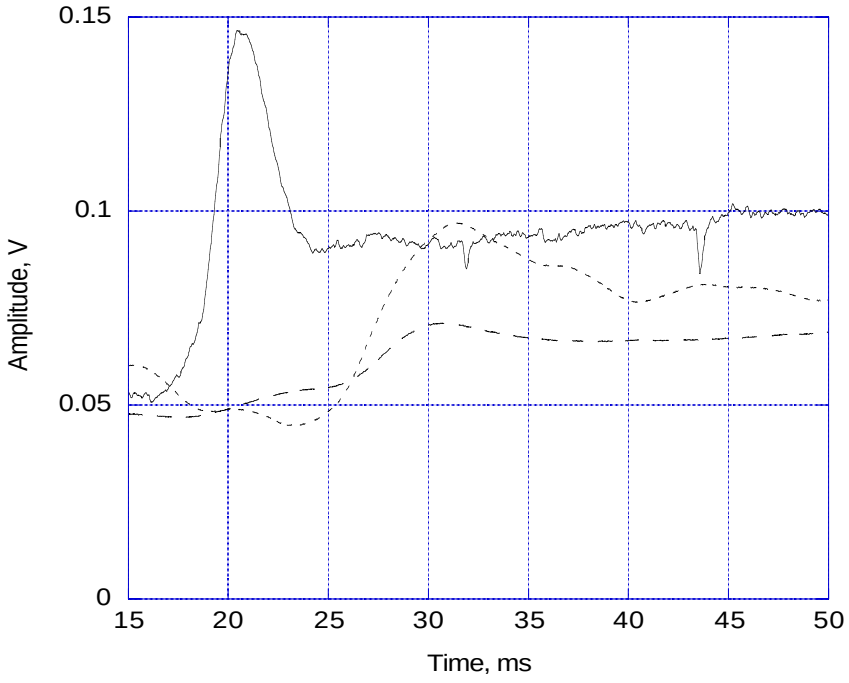

Figure 4. Negative-ion spectra produced by corona discharge in air (– – –) and simulated exhaust gas (----) and by spark discharge in simulated exhaust gas (—).

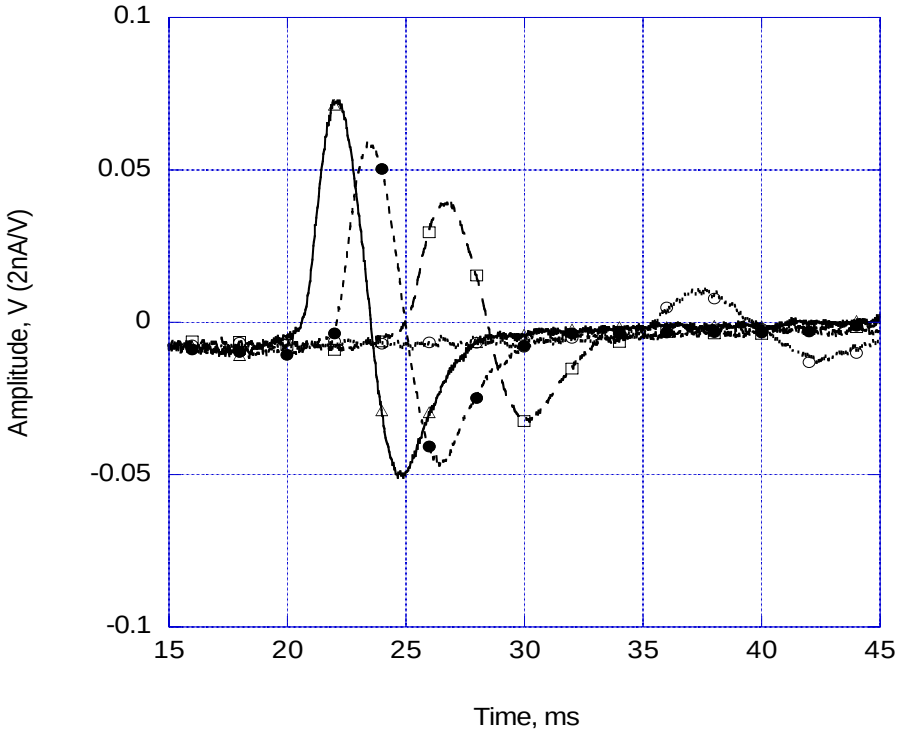

Figure 5. Evolution of negative-ion peak (from high, -o-, to low, -Δ-, drift time) produced under spark discharge mode after ion source is turned on.

2.4.2 Flow Effects

Because our IMS sensor is basically designed for ambient operation, temperature and pressure in the ion drift tube are assumed to be constant; thus, minimal effects are expected on the spectra. Only the flow effect was examined. Flow can be introduced parallel with the negative-ion drift direction (forward flow) or from the opposite direction (counterflow). Figure 6 shows the effect of flow direction on the negative-ion peak. Counterflow not only slows down ion drift time but also increases peak amplitude. The changes are certainly not caused simply by the gas flow rate (180 cm^3/min) but most likely are due to the initial position of the ions, because the small drift time shift (≈ 0.94 ms) corresponds to a distance of 0.36 cm. The amplitude increase may be due to increased ion concentration in the ionization cell. Figure 7 shows the effect due to plugged flow, created by plugging the flow outlet while introducing 200 cm^3/min counterflow of dry nitrogen. Increased drift time and broadening of the peak were observed, which may be attributed to a slight increase in pressure that led to increased ion diffusion time.

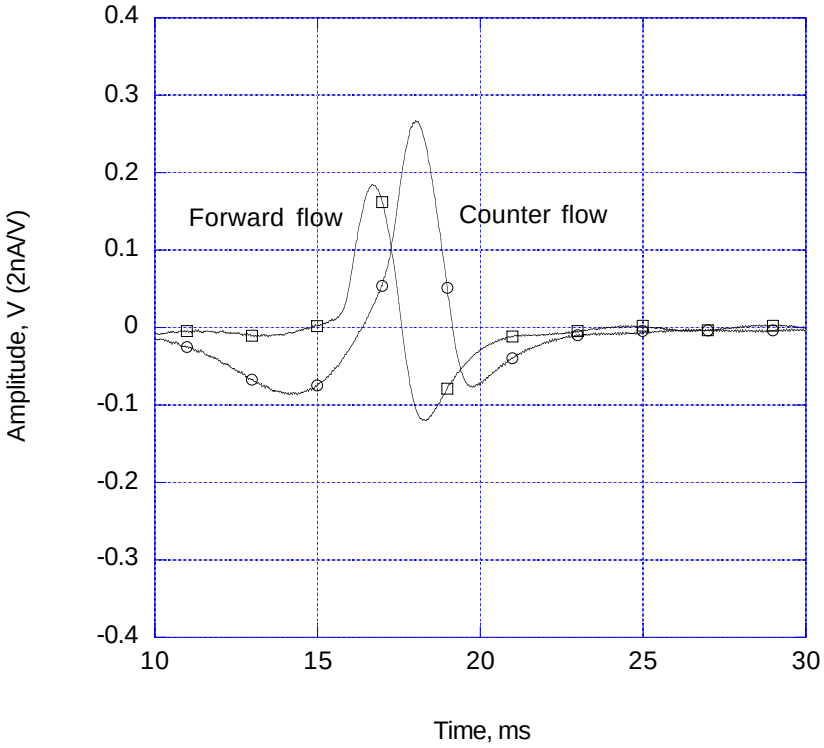

Figure 6. Effect of flow direction on negative-ion peak.

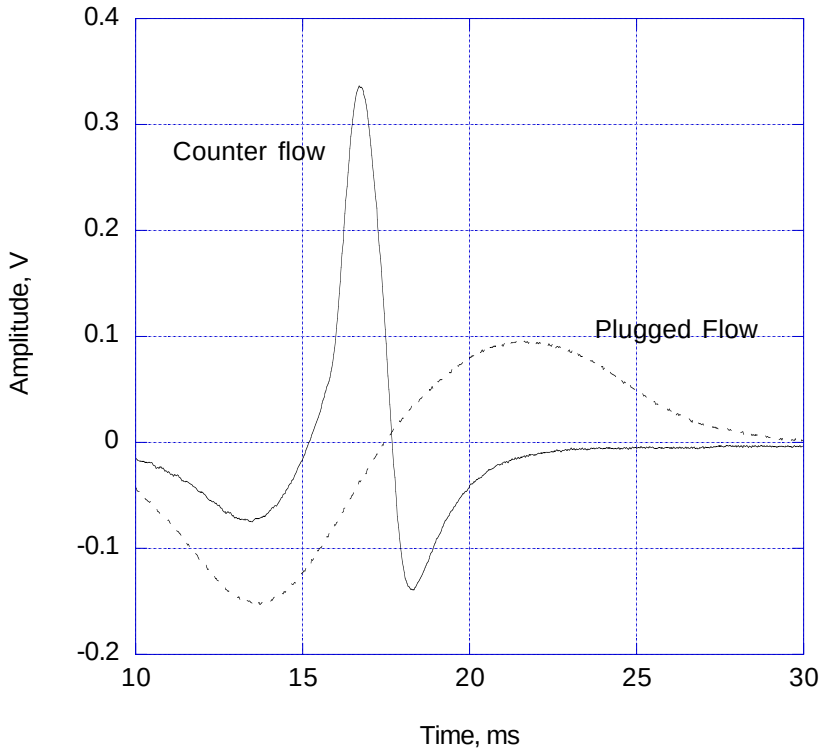

Figure 7. Effect of flow on negative-ion peak.

2.4.3 Moisture Interference

The presence of water vapor in the IMS sensor tends to degrade the ion spectrum. Figure 8 shows the extent of degradation of the NO_2 ion spectra of gas mixtures that contain various water vapor concentrations. In most cases, we found that the ion spectrum was completely masked by noise when the vapor content exceeded 1%. Therefore, a method to reduce the noise is necessary for practical applications. Two techniques were examined for removing moisture from the gas stream. One, based on the thermoelectric Peltier effect, condenses water vapor before the gas enters the sensor. Figure 9 shows three ion spectra obtained when vapor-saturated gas was passing through the cold side of a Peltier plate at the indicated temperatures. The spectra show that, as temperature decreases, the signal-to-noise ratio improves and the delay time of the peak decreases. The changes in delay time suggest that the size of a water cluster may be reduced as temperature decreases. In the other technique, a polymer membrane (Nafion® tube) is used to separate water moisture from the gas stream. Nafion tubing consists of Teflon with sulfuric acid groups interspersed within it. Because the affinity of sulfuric acid for water is very high, Nafion tubing absorbs water. The absorbed water then diffuses through the tubing, depending on the difference of the water vapor pressure across the tubing. To demonstrate this function, we pass nitrogen gas with ≈1% water vapor inside the Nafion tubing and dry nitrogen outside the tubing. Figure 10 shows the difference in the two ion spectra. Use of Nafion tubing in front of the ionization cell, indeed, can recover the ion peak.

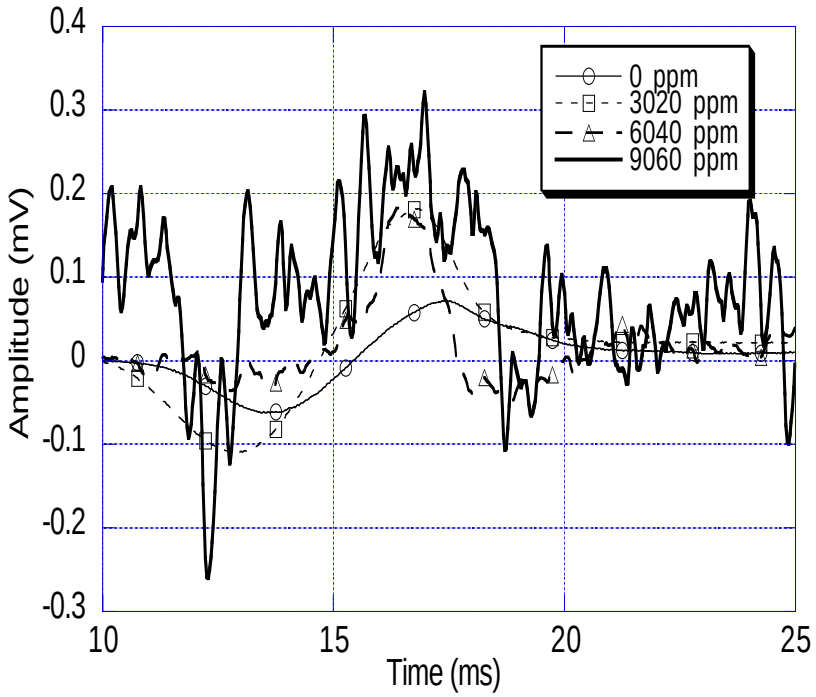

Figure 8. NO_2 ion spectra of NO_2/simulated exhaust-gas mixtures with various water vapor concentrations.

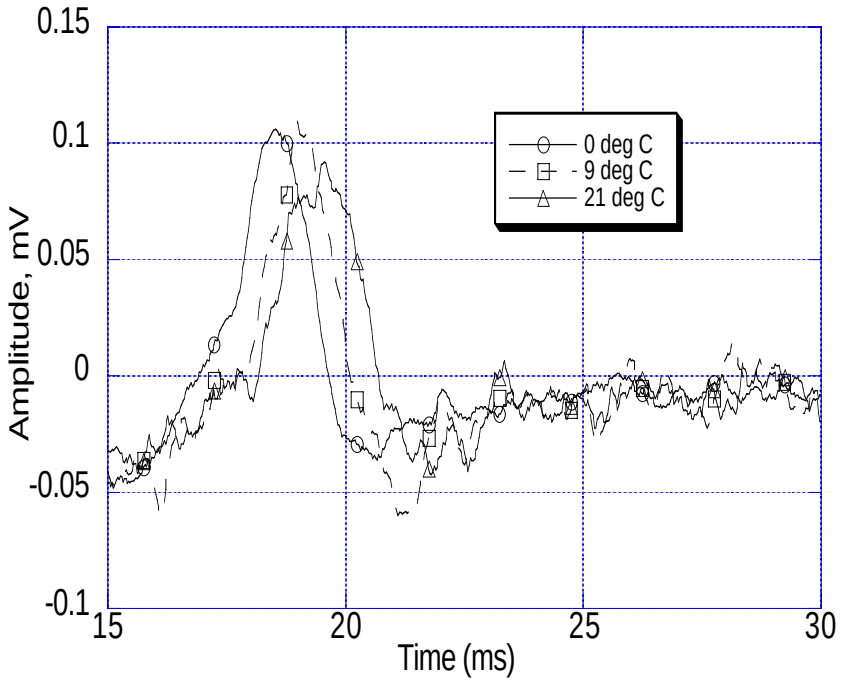

Figure 9. Negative-ion peaks detected by controlling carrier-gas temperature.

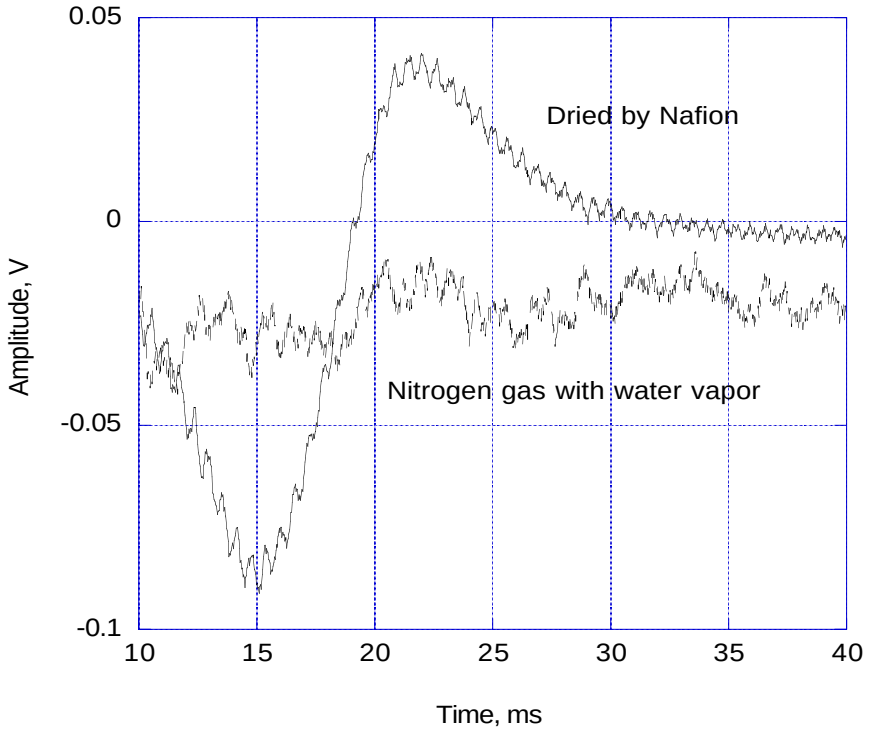

Figure 10. Negative-ion spectra of nitrogen gas before and after water vapor flow passed through a Nafion tube.

2.4.4 Ion Chemistry

Dry nitrogen does not produce negative ions under either corona or spark discharge. However, if oxygen is present in the ionization cell, negative O_2^- or O_3^- and NO_2^- may be produced. As one introduces NO_x into the cell, both NO^- and NO_2^- will be produced, with the latter dominant, based on the larger electron affinity of NO_2. Figure 11 shows the spectra of three nitrogen/NO_x mixtures. Both peak amplitude and drift time increased with NO_x concentration. The results suggest that the spark-discharge mode of operation may be used to quantify NO_x concentration by measuring the peak amplitude and drift time.

Based on electron affinity, one expects to detect negative O_2^-, O_3^-, and SO_2^- ions when simulated exhaust gas is used as the carrier gas. However, because of poor resolution, current IMS detected only one broad peak at a relatively high drift time. Figure 12 shows the ion spectrum of the simulated exhaust gas and a spectrum of a mixture that contained 83 ppm NO_2. The presence of NO_2 shifts the peak to a lower drift time, suggesting the presence of NO_2^-.

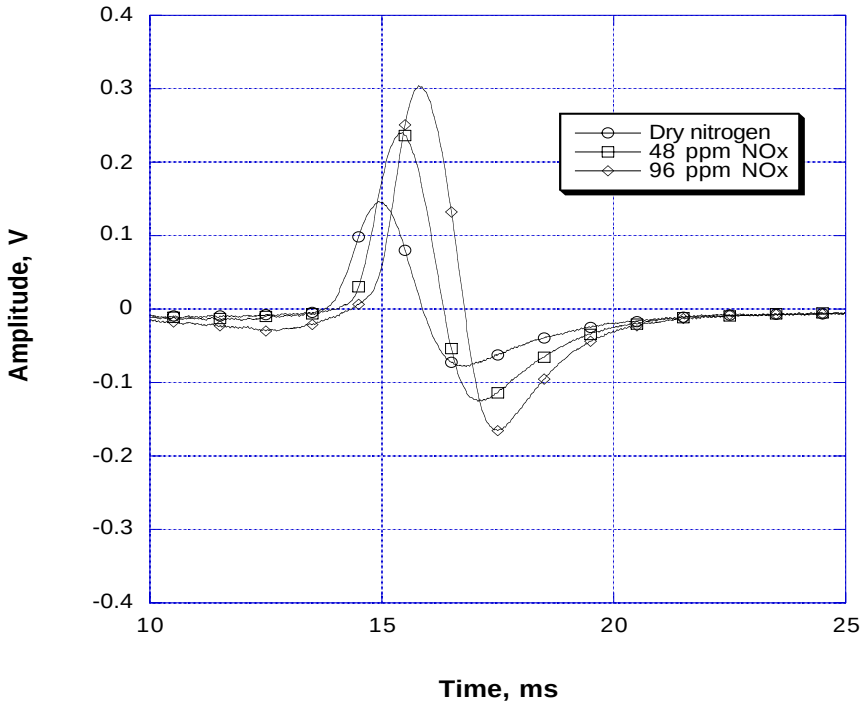

Figure 11. Negative-ion spectra for dry nitrogen and nitrogen/NO_x mixtures.

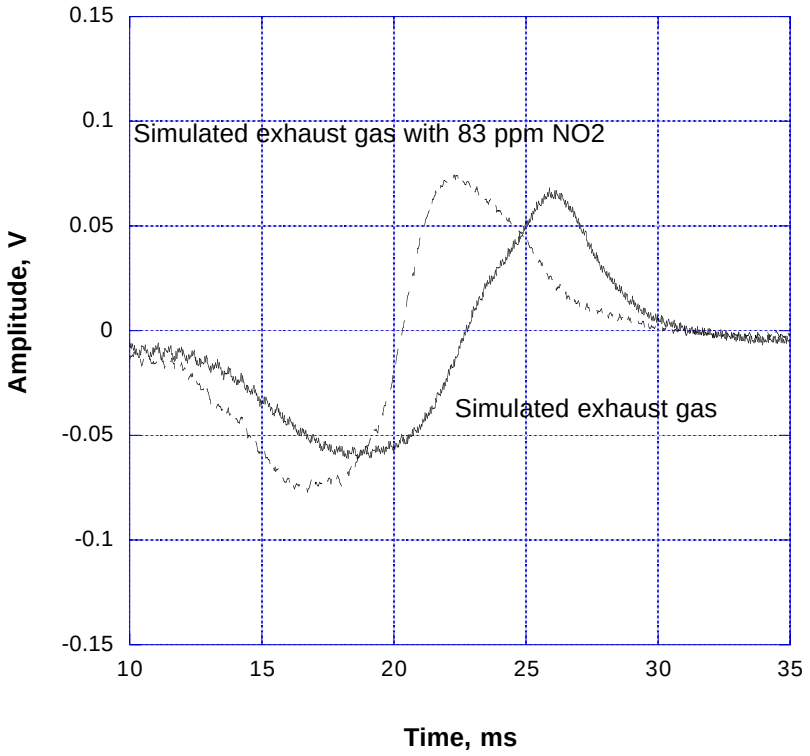

Figure 12. Negative-ion spectra for zero and 83 ppm NO_2 in simulated exhaust gas.

When He gas was used as the carrier gas, we detected a large ion peak at ≈7 ms drift time. The peak is believed to be He^- [22]. Because the electron binding energy of He (0.076 eV) is low, it tends to lose an electron to NO_x through ion-molecule interaction. In Fig. 13, which shows the spectra of NO_x/N_2/He mixtures, we find that, as NO_x increases, the peak amplitude decreases but the drift time increases. This finding supports the fact that when He is the carrier gas, the primary reaction is the charge exchange between He^- and NO_x.

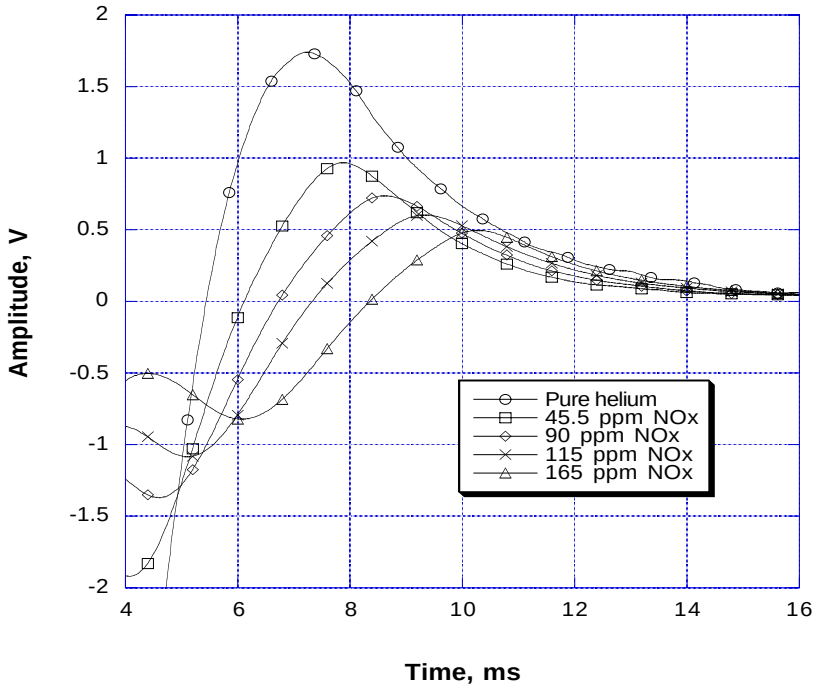

Figure 13. Negative-ion spectra of $He/NO_x/N_2$ gas mixtures.

We also examined the use of argon gas (Ar) as the carrier gas. It is known that Ar does not form negative ion [22]. Thus, when Ar is the carrier gas, the only possible reaction upon introduction of NO_x will be direct electron attachment. Figure 14 shows the spectra of three $NO_x/N_2/Ar$ mixtures; indeed, no peak was detected with pure Ar gas and a broad peak at high drift time was measured when NO_x was introduced. The high drift time may be due to the large collision cross section between NO_x and Ar.

2.4.5 NO_x Detection

The IMS sensors we have developed uses a spark-discharge ionization source and operates in negative-ion mode under ambient conditions. Although only one peak can be resolved for NO_x regardless of the composition of NO_x and carrier gas used, the sensor we developed can provide a quantitative measure of NO_x. The NO_x measurement can be based on changes of peak amplitude, drift time, or discharge current. Among the three, drift time variation is relatively small. Figure 15 shows the ion spectra of various NO_x concentrations.

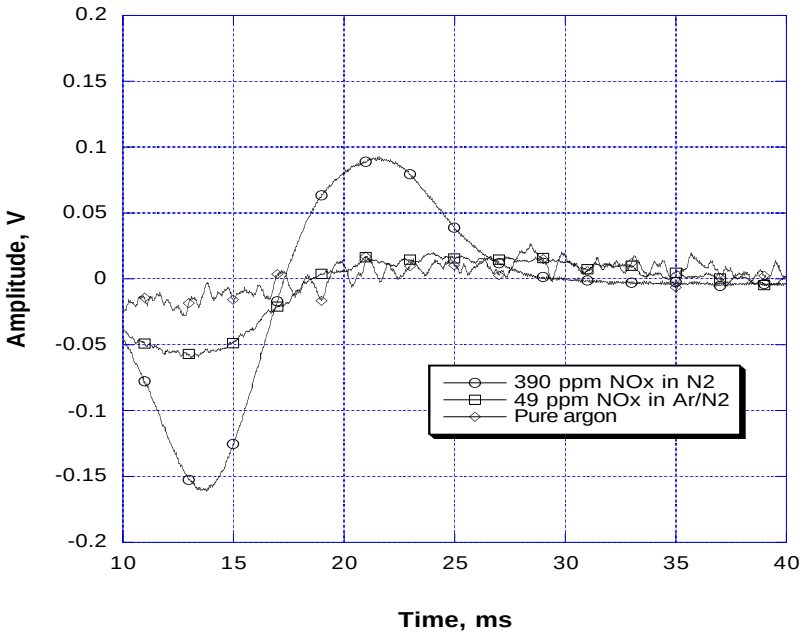

Figure 14. Negative-ion spectra of $Ar/NO_x/N_2$ gas mixtures.

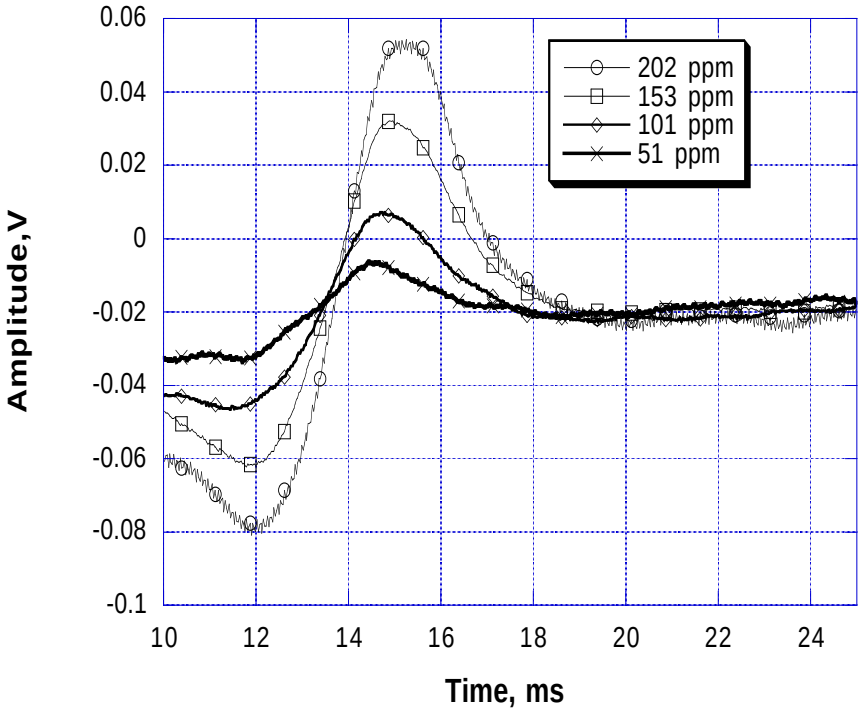

Figure 15. Negative-ion spectra of various NO_x concentrations (operating setup: -3.4 kV, 200 sccm, and 1 nA/V).

As shown in Fig. 15, the amplitude change provides better sensitivity in NO_x. Figure 16 shows peak amplitude as a function of NO_2 concentration, measured with dry nitrogen as the carrier

gas. When simulated exhaust gas was used as the carrier gas, the NO_x^- peak amplitude, as shown in Fig. 17, also increased with NO_x concentration. In both cases, the estimated accuracy is 10%.

In the spark-discharge mode, the current passing from the needle to the shell surface is relatively high (>0.6 mA with –3.6 kV applied voltage). The measured current is primarily due to electron flow. When NO_x gas is introduced, a portion of the electrons will interact with NO_x molecules and thus reduce the current. Figure 18 shows the changes of spark-discharge current for various NO_2 concentrations. A linear dependence with negative slope is measured.

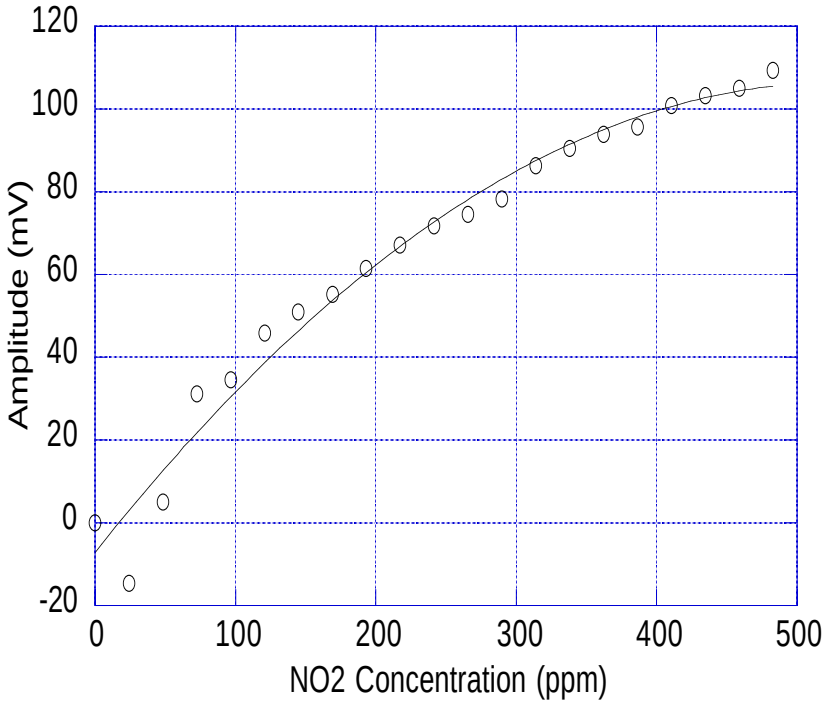

Fig. 16. Peak amplitude vs. NO_2 concentration, measured in presence of dry nitrogen and at 2 nA/V sensitivity.

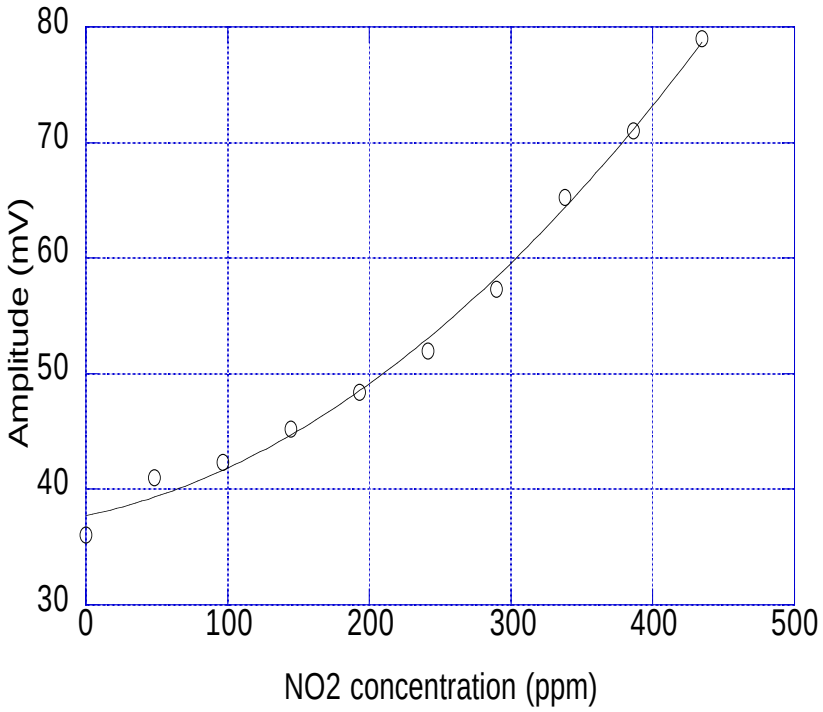

Figure 17. Peak amplitude vs. NO_2 concentration, measured in presence of simulated exhaust gas and at 5 nA/V sensitivity.

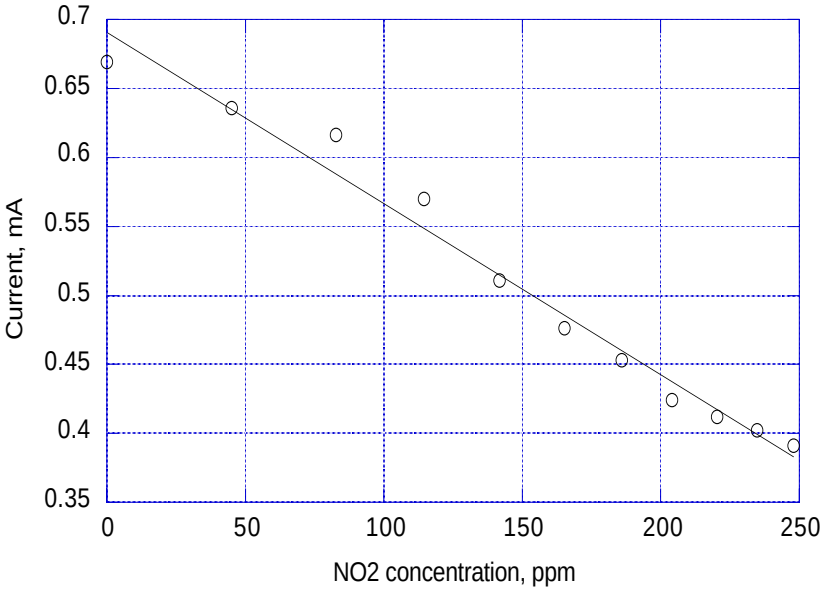

Figure 18. Spark-discharge current vs. NO_2 concentration.

2.5 Status and Proposed Future Development

The targeted real-time NO_x emission sensor must give a fast response and demonstrate high sensitivity to NO_x emissions in the range of 1-100 ppm. The sensor must be able to function under an ARES engine exhaust environment that is typically at high temperature and contains more than 10% moisture. The status ANL's IMS NO_x sensor is outlined below:

- A nonradioactive spark-discharge ionization source was successfully developed and demonstrated;
- A laboratory prototype was built and tested. Negative NO_2 ions are the primary ions detected in the two carrier gas streams, dry nitrogen and simulated exhaust gas;
- Negative-ion current intensity can be correlated with both NO_2 and NO_x concentrations up to 200 ppm with high sensitivity and linear dependence; and
- The effect of water vapor on IMS spectra and methods to reduce the effect were examined.

The laboratory laboratory takes 80 ms to complete a sweep. Typically, on average, over 100 sweeps are required to resolve a spectrum; thus, the present IMS sensor can produce a measurement in less than ten seconds, depending on the speed of the data acquisition system. However, the present prototype is not ready for field applications because

- Its ion drift tube is cumbersome to build (40 resistors in series);
- Its sensitivity varies with gas composition, especially the presence of moisture and particulate matter (PM);
- The signal-to-noise ratio may be affected by the sensing environment, especially mechanical vibration;
- The control system consists of expensive laboratory electronic equipment;
- The cost is still high.

To overcome the aforementioned drawbacks, we propose the following developments.

2.5.1 Design of a High-Temperature Drift Tube

Design of the drift tube is critical to the performance of the IMS sensor. A uniform electrical field is essential to the ion trajectory. The currently used typical arrangement relies on a series of resistors of equal value to separate the metal rings that surround the glass or ceramic tube, and the current design, in addition to its complexity in fabrication, cannot be applied to high-temperature environments because of the resistors. Therefore, the proposed research will evaluate various materials, such as conductive ceramics or composites, which can behave as a high-resistance conductors at high temperatures. An ion drift tube made of such a material will not require resistors to establish a uniform field; thus, the design will be simplified and the cost reduced. Conductive polymer tubes are commercially available (e.g., Vespel SP-22 by DuPont).

Use of a conductive polymer to establish a uniform DC field has been demonstrated in a time-of-flight mass spectrometer design [23], however, such polymers may have an upper temperature limit (<300°C). Therefore, for operation at higher temperature, it may be necessary to use conductive ceramics that generally decrease resistance as temperature increases.

2.5.2 Design of the Front-End Gas Sampling System

Although the corona/spark-discharge IMS sensor, when operated in negative-ion mode, responds primarily to NO_x, the presence of moisture and PM will shift the drift time and reduce the amplitude. We also found that more averages are needed because of poor S/N ratio. To improve performance, we propose to develop a gas sampling system that will condition the exhaust gas for the sensor. Design of the system will be based on two concepts. One is the use of Nafion tubing to remove the moisture from the exhaust gas, the other is the use of another stage of corona discharge ionization to remove positive ions that are mostly water and PM clusters.

2.5.3 Design of an Integrated Electronic Package

The control electronics have been partially designed. We need to add to the present electronics a band-passed charge amplifier (to eliminate vibration noise), and the data acquisition and analysis μ processor.

2.5.4 Design of a Low-Cost NO_x Sensor

Based on the correlation between the spark-discharge current and NO_x concentration, a low-cost NO_x sensor can be built. However, additional research is needed to establish the required ion equilibrium conditions inside the discharge source so a constant current can be established for each NO_x concentration.

3.0 ACOUSTIC NATURAL-GAS SENSOR

The typical fuel gas composition of a natural-gas reciprocating engine consists of 82-96% methane, 2-7% ethane, 0.4-1.1% propane, and up to 0.6% higher hydrocarbons. To optimize combustion efficiency and reduce NO_x emissions one needs to control the fuel input to the natural-gas combustion engine. Such control requires real-time measurement of mass flow rate and gas composition; real-time measurement, in turn, requires a sensor with a fast response and quick recovery time. Semiconductor sensors [24] generally cannot fulfill the requirements. Acoustic gas sensors that use airborne sound properties [25] have been investigated for potential industrial online gas analysis. The typical properties that are measured by these sensors are sound speed and attenuation. The advantages of an acoustic sensor are fast response, robustness, and low cost; the drawbacks are poor sensitivity and applicability primarily to binary gas mixtures. The development under this project focused on acoustic methods to measure intake gas composition.

3.1 Phenomenological Model

For a binary gas mixture, a simple sound velocity measurement can determine the composition. But for multicomponent gas mixtures, additional independent measurements are required. The additional measurement could be the attenuation, even though acoustic attenuation is generally related to velocity dispersion and can be derived from phase velocity through Kramers-Krong relationships [26]. But, in practice, one can only measure phase velocity or attenuation over a finite frequency range. Therefore, sound velocity and attenuation may be considered two independent parameters. Thus, assuming that sound velocity and attenuation are independent parameters, we developed a phenomenological model. The measured sound velocity (V) in a gas is pressure dependent, can be related to a second virial coefficient, and can be given by [27]

$$V = V_i(1 - \beta p), \tag{4}$$

where p is pressure, ß is a function of the second virial coefficient of the gas, R is the gas constant, T is the absolute temperature, and V_i is the ideal-gas sound velocity given by

$$V_i = \sqrt{\frac{\gamma RT}{M}}, \tag{5}$$

where γ is heat capacity ratio and M is the molecular weight of the gas. For a gas mixture such as natural gas, sound velocity at a given temperature and pressure, in principle, can be calculated from

$$V(p,T) = \sqrt{\frac{\sum_{j=1}^{n} \phi_j \gamma_j RT}{\sum_{j=1}^{n} \phi_j M_j}} \left(1 - \sum_{j=1}^{n} \phi_j \beta_j p\right), \tag{6}$$

where β is a small variable that depends on the second virial coefficient of the gas, ϕ_i is the volume fraction of the gas constituent i, and $\sum_{j=1}^{n} \phi_j = 1$. Because a typical natural gas contains more than 90% methane, one may approximate the sound velocity of the natural gas by the simple combination of the constituents' sound velocities, given as

$$V = \sum_{j=1}^{n} \phi_j V_j . \tag{7}$$

The sound velocity calculated from Eq. 6 differs slightly (<10%) from the direct linear combination of individual sound velocities, Eq. 7. Table 2 lists some of the parameters of

nitrogen and of the three major constituents of natural gas. Note that sound velocity of methane is ≈25% higher than the velocity of other gases, which provides good sensitivity when monitoring methane concentration.

Table 2. Speed of sound, heat capacity, and virial coefficient of natural-gas constituents

Gas parameter	methane	ethane	propane	nitrogen
ß	0.000424	-----	-----	-0.000057
C_p, J/deg-mol[a]	35.7	52.5	73.6	29.124
V_i , m/s[b]	446	316	253	346

[a]Lange's Handbook of Chemistry, 15th edition, McGraw-Hill, Inc. 1999.

[b]CRC Handbook of Tables for Applied Engineering Science, 2nd edition, CRC Press, 1973.

Acoustic attenuation (α) in a gas under isentropic conditions, primarily the result of effects due to viscosity drag and heat conduction, is commonly referred to as classical attenuation α_{cl}, expressed in Eq. 8 in terms of a dimensionless μ_{cl} (= $\alpha_{cl}\lambda$, where λ is wavelength) and frequency over pressure, *f/p*:

$$\mu_{cl} = \frac{2\pi^2}{\gamma}\left[\frac{4}{3}\left(\eta + \frac{3}{4}\eta'\right) + \frac{\kappa(\gamma-1)}{C_P}\right]\frac{f}{p}, \tag{8}$$

where C_P is the heat capacity at constant pressure of the gas; and η, η', γ, and κ are shear viscosity, bulk viscosity, heat capacity ratio, and thermal conductivity of the gas respectively. The expression clearly shows that the dimensionless attenuation increases monotonically with *f/p*. Rigorously, acoustic attenuation in a gas mixture can be calculated from Eq. 9 with linearly combined individual physical parameters, as was done in Eq. 6. With <10% ethane and other hydrocarbons, the attenuation in a natural gas may be estimated from Eq. 9.

$$\mu(f/p) = \sum_{j=1}^{n} \phi_j \mu_j (f/p), \tag{9}$$

where *f* is the frequency of the ultrasound. The attenuation calculated by Eq. 9 is slightly overestimated.

The classical attenuation in an atomic gas, such as rare gases, represents the total energy absorbed by the gas. But for gases of molecules that contain more than one atom, other degrees of freedom are present that will absorb energy and provide more attenuation. These degrees of freedom, due to transitions of internal states of the molecule, involve mainly vibrational and

rotational states when acoustic waves propagate in the gas. Typically, molecules will absorb the acoustic energy and return the energy later in the wave cycle. The phenomenon is called acoustic relaxation [28], which is an irreversible thermodynamic process that transfers energy from the translational mode of motion to the internal modes of the molecule, or to the potential energy of some structural rearrangement. This energy, being absorbed by the gas molecules, reaches its highest value per period when the length of a period approximately equals the time required to achieve equilibrium. Therefore, for different polyatomic molecules there exist different acoustic relaxation spectra [29] which may be used to identify gas molecules.

In principle, the acoustic relaxation problem can be solved by irreversible thermodynamics, kinetic theory, or statistical mechanics. The latter two require rigorous analysis based on collision dynamics and quantum mechanics, and, for most cases, become an insurmountable problem. Irreversible thermodynamics has been thoroughly examined [30] and verified by measurements. The theory generates phenomenological expressions for acoustic attenuation (Eq. 10) under irreversible relaxation processes:

$$\mu_R = \frac{\pi\varepsilon}{\sqrt{1-\varepsilon}} \frac{\omega\sqrt{\tau_{PS}\tau_{VS}}}{1+\omega^2\tau_{PS}\tau_{VS}}. \tag{10}$$

Here, C_o is the isentropic sound speed, μ_R is the dimensionless attenuation due to relaxation, ε is the relaxation strength, and τ_{PS} and τ_{VS} are the adiabatic relaxation times at constant pressure and volume, respectively. From Eq. 11, one can derive the maximum attenuation.

$$\mu_{\max} = \frac{\pi\varepsilon}{2\sqrt{1-\varepsilon}}, \tag{11}$$

which occurs at

$$\omega_{\max} = \frac{1}{\sqrt{\tau_{PS}\tau_{VS}}}. \tag{12}$$

In general, relaxation time is inversely proportional to pressure. Hence, attenuation data are normally plotted as μ vs. *f/p*. By combining Eqs. 10-12, we obtain

$$\mu_R = 2\mu_{\max}\left[1+\frac{(f/p)^2}{(f/p)^2_{\max}}\right]^{-1} \frac{(f/p)}{(f/p)_{\max}}. \tag{13}$$

Both μ_{max} and $(f/p)_{max}$ can be obtained from measurements, for example, the relaxation peak for methane was reported *f/p = 0.2* MHz/atm [31, 32]. The total acoustic attenuation of a gas is then the sum of classical and relaxation attenuation.

3.2 Sensor Design and Experiments

The basic design of the prototype acoustic gas sensor consists of a pair of air-coupled transducers mounted face-to-face in a hermetically sealed chamber. The separation between the transducers is ≈3.986 cm, determined by measuring the speed-of-sound in dry nitrogen. Figure 19 shows a schematic diagram of the laboratory setup for sensor evaluation. Temperature and pressure inside the chamber were also measured during the tests. The sensor operates in pitch-catch mode. Gated sine waves of a fixed frequency (0.1 - 0.5 MHz) were used to excite the transmitter. Because a narrow flow channel was used, the receiver detected multiple reflections. The echo train was analyzed for variations in amplitude and time-of-flight, from which attenuation and speed of sound were determined. Two types of transducers were tested, 0.5 MHz (Etalon, a Division of Piezo Technologies) and 0.2 MHz (AT-200 by AIRMAR Technology Corporation).

Sensor tests were conducted with pure methane, ethane, propane, nitrogen, and their mixtures. To measure relaxation peaks, we conducted the tests with a range of f/p, which was achieved by either varying the gas pressure or changing the wave frequency. The pressure tests were performed either by establishing an equilibrium pressure or by continuous pressure decay from high pressure to ambient. The frequency change was somewhat limited because the same set of transducers was used. The accessible frequencies were determined from their signal-to-noise ratios.

Figure 20 shows a typical pulse train detected by the receiver. A peak detector was used to locate the peak maxima and their amplitudes. The time difference of two consecutive peaks corresponds to the transit time over a distance of two times the transducer separation; thus, it determines the sound velocity. The decay of the peak amplitude was fit with an exponential decay function, from which the attenuation was determined.

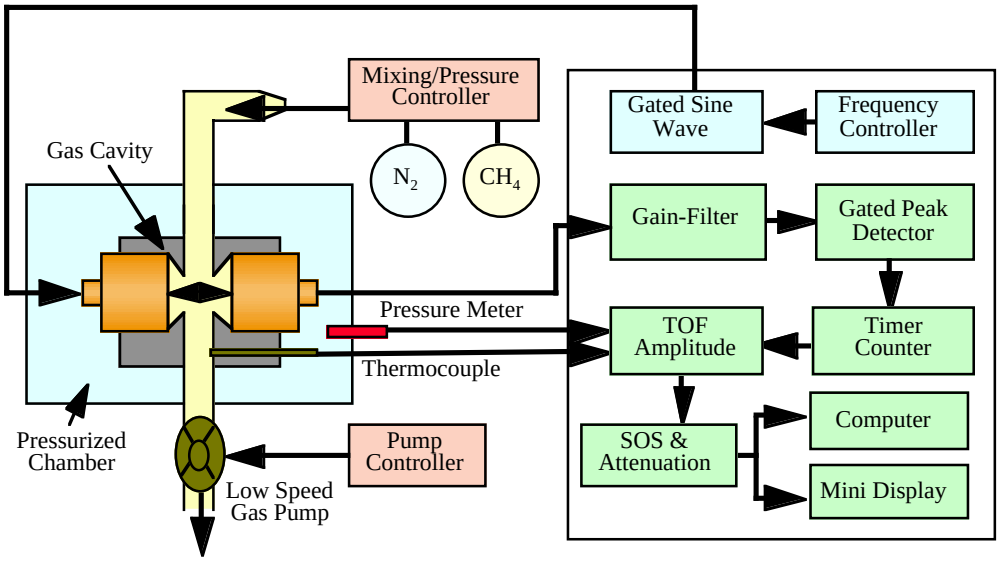

Figure 19. Schematic diagram of laboratory prototype of acoustic sensor and associated control electronics and processing system.

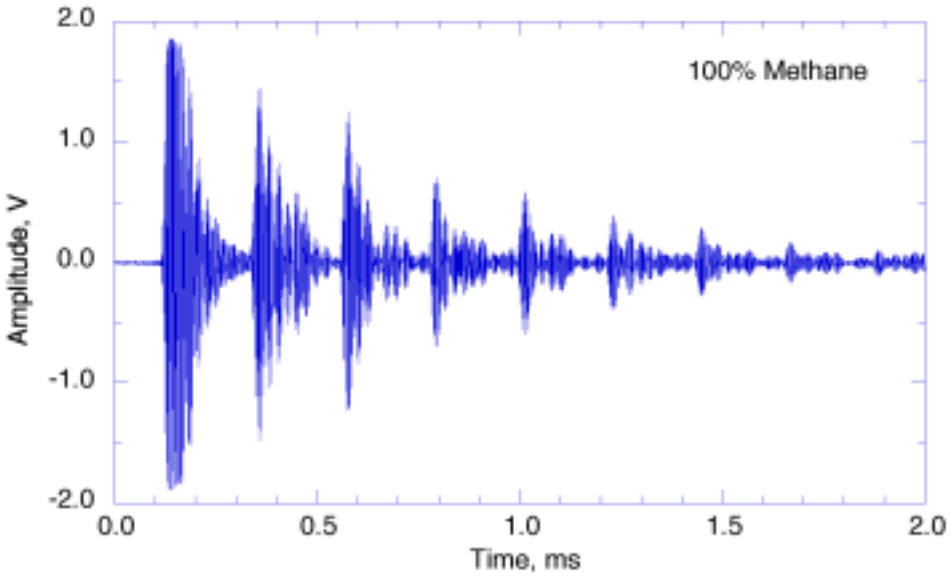

Figure 20. Pulse train detected in methane when f/p = 125 kHz/atm.

3.3 Results and Discussion

A recent theoretical prediction [33] and experimental measurement [34] of relaxation spectra of methane show a peak near f/p = 0.1 MHz/atm. The peak shifts its position when a second gas such as nitrogen is introduced. Inasmuch as our goal is to develop a natural-gas sensor, our tests

focused on variations in acoustic properties over a range of *f/p* that covered the resonance peak of methane. Therefore, the results given in this section include the speed of sound and attenuation of natural-gas mixtures in the region of $f/p < 0.5$ MHz/atm.

3.3.1 Speed of Sound

Figure 21 shows pressure-dependent sound velocities for nitrogen, methane, ethane, and propane. Sound velocity at each pressure was also measured with various ultrasonic frequencies (170– 470 kHz). Very little velocity dispersion was measured over the tested frequency range. But, it should be noted that the measured sound velocities are, indeed, pressure dependent even though the dependency is very small. For dry nitrogen, we obtain a slope of 0.00004 (or $\beta = -0.00004$) as compared with the reported virial coefficient –0.000057 given in Table 2. But, for methane, ethane, and propane, the pressure dependency is nonlinear. However, the pressure-dependent coefficients (β) can be deduced from parts of the curves. The β for methane at a pressure <2 atm is a negative value, which is the opposite of the reported value given in Table 2. But positive values can be deduced for ethane and propane.

For binary gas mixtures, changes in the speed of sound (SoS) can be used to determine the gas composition, especially, when the difference between the SoS of two gases is large. The technique has been demonstrated and optimized in a recently developed helium leak detector [35]. In Fig. 22, we show the SoS variations for three binary gas mixtures of methane. Along with the data, we also plot the calculated SoS changes from Eqs. 6 and 7. Equation 6 shows a better fit to the ethane/methane data whereas Eq. 7 gives a perfect fit to the propane/methane data. The nitrogen/methane data, taken with $f/p = 0.49$ MHz/atm, deviate from both calculated values in the region of 20-40% methane. However, Eq. 7 can be used to monitor natural-gas composition that contains >90% methane. The estimated resolution for ethane/methane mixtures is ≈1% composition change, which corresponds to 1 m/sec of SoS change.

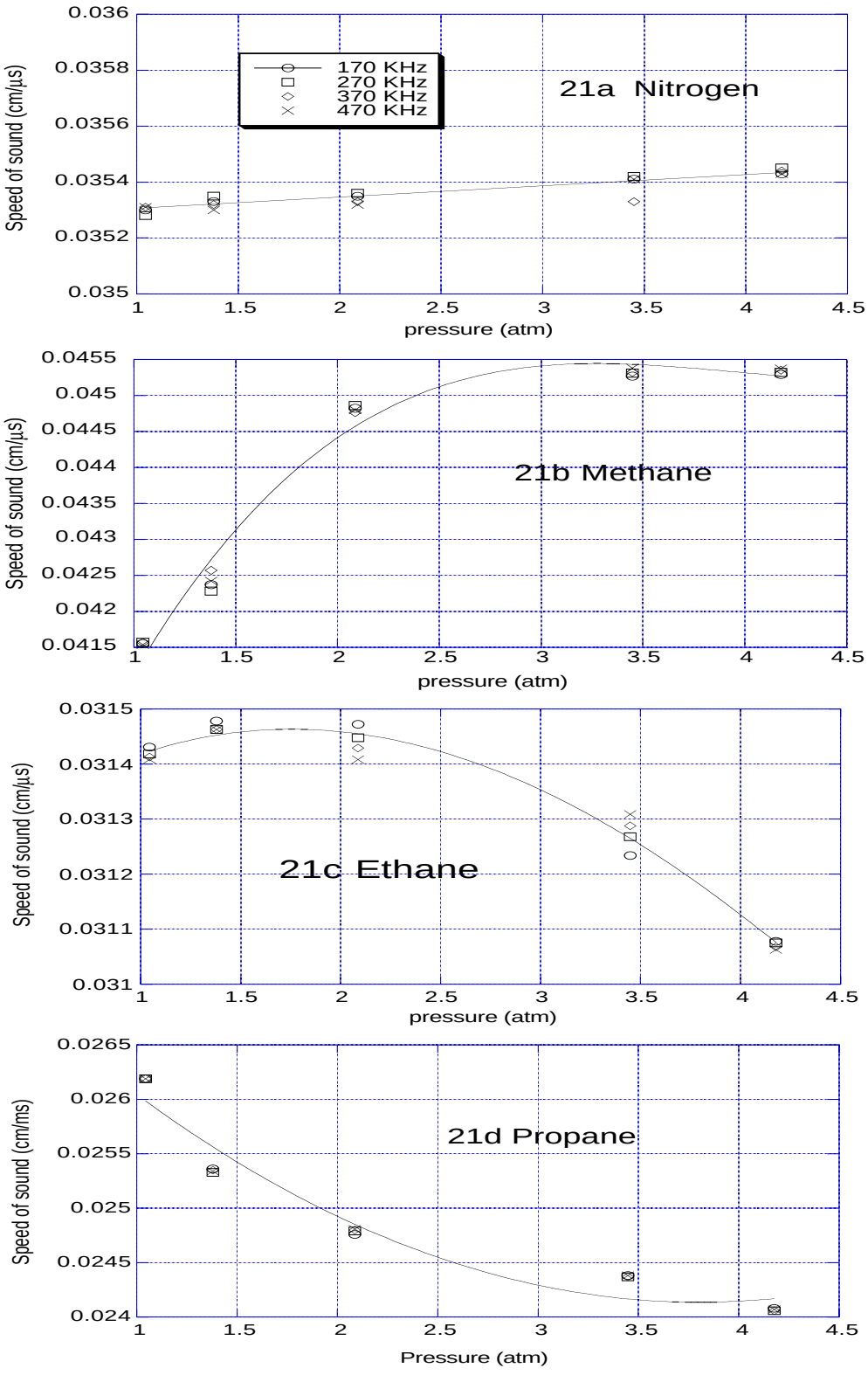

Figure 21. Speed of sound vs. pressure for nitrogen, methane, ethane, and propane. Solid lines represent best-fit curves.

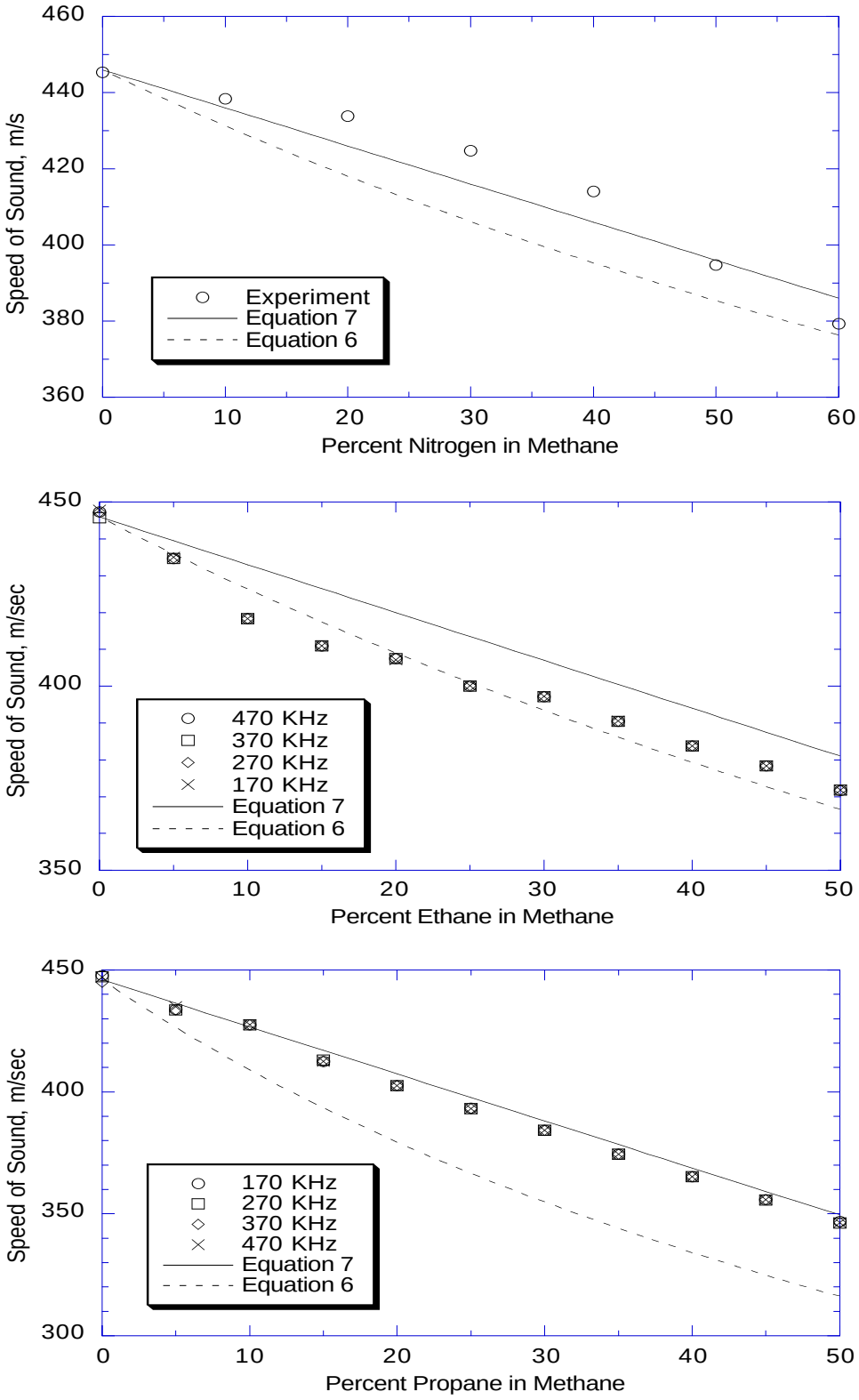

Figure 22. Speed of sound for binary gas mixtures.

3.3.2 Acoustic Attenuation

Absolute acoustic attenuation is very difficult to measure. For acoustic waves propagating in a gas mixture, attenuation is present that is due to viscosity and thermal effects (the so-called classical attenuation), to relaxation of the vibrational and rotational states of the gas molecules (relaxation term), and to the gas diffusion effect. For natural-gas mixtures, the gas diffusion effect may be neglected because the difference in molecular weight from methane to propane is relatively small. Two other effects also attenuate the signals, one is due to diffraction, the other is the system loss due to impedance mismatch between the transducer and gas. The pitch-catch method employed in our measurement generates a minimal loss (<0.5%) from both the diffraction and system losses. Our attenuation measurements cover an *f/p* range from 0.05 to 0.5 MHz/atm. In this range, an acoustic relaxation peak was observed for methane. Figure 23 shows the dimensionless attenuation as a function of *f/p* in a 1:1 mixture of nitrogen/methane. A relaxation peak at $f/p \approx 0.06$ MHz/atm is detected. The solid line, the prediction from Eq. 13 when the experimental values of $(f/p)_{max}$ and μ_R are used, shows a slow decay of the relaxation process. To fit the data, we obtain an empirical expression given as Eq.14 and plotted as the dashed line in the figure:

$$\mu_R = 2\mu_{max}\left[\frac{f/p}{(f/p)_{max}}\right]^2 \exp\left\{-\left[\frac{f/p}{(f/p)_{max}}\right]^2\right\}. \qquad (14)$$

In Fig. 24, we show the acoustic attenuation for pure methane, pure ethane, and a methane/ethane (0.9:0.1) mixture. Again, the pure methane showed a relaxation peak at $f/p \approx$ 0.05 MHz/atm, slightly shifted to a lower *f/p* as compared to the (1:1) methane/nitrogen mixture. The peak was shifted to higher values of *f/p* when ethane was introduced. The relaxation peak for pure ethane was not resolved very well but its existence was detected. The data also show that the attenuation in an ethane/methane mixture falls between the attenuation in methane and ethane, but it may not provide a direct quantitative measure of the gas composition.

In Figs. 25 and 26, we show the acoustic attenuation per wavelength vs. gas composition for ethane/methane and propane/methane mixtures, respectively. The attenuation data were obtained at four ultrasonic frequencies. Overall, we found that the acoustic attenuation decreased as ethane or propane concentration increased, and that rather steeper changes in attenuation were detected at lower concentrations of ethane or propane gas. Thus, the data suggest that the attenuation measurement may be sufficiently sensitive to detect changes in natural-gas composition.

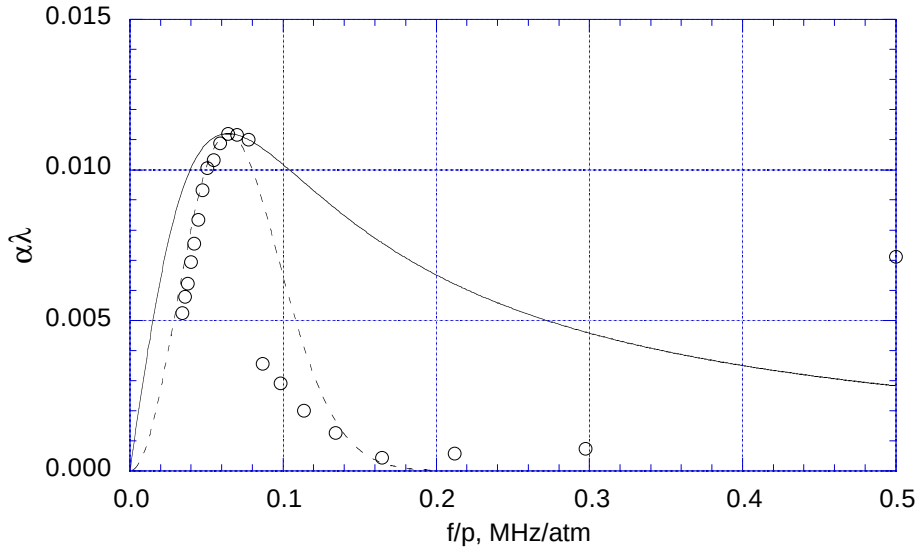

Figure 23. Attenuation per wavelength vs. frequency over pressure in methane.

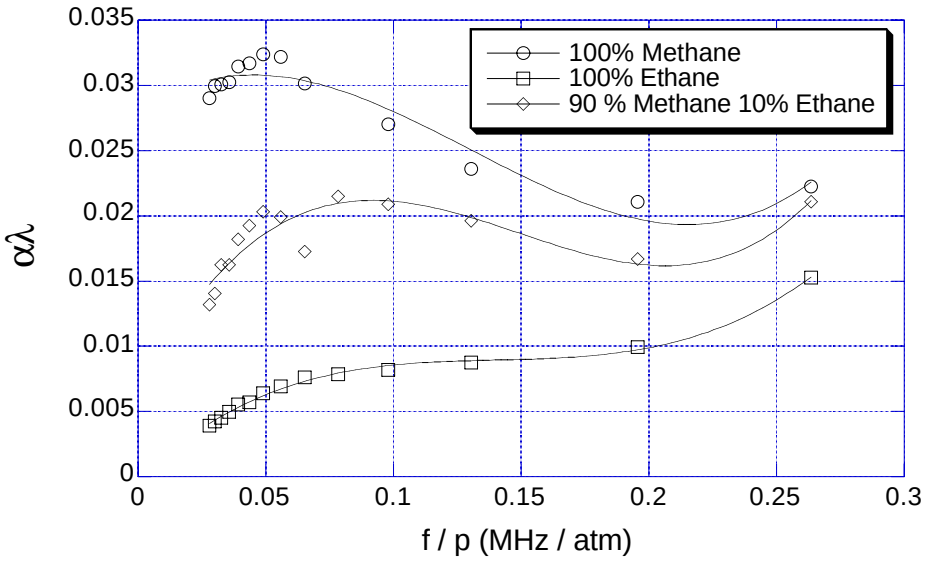

Figure 24. Attenuation per wavelength vs. frequency over pressure in methane, ethane, and methane/ethane mixture.

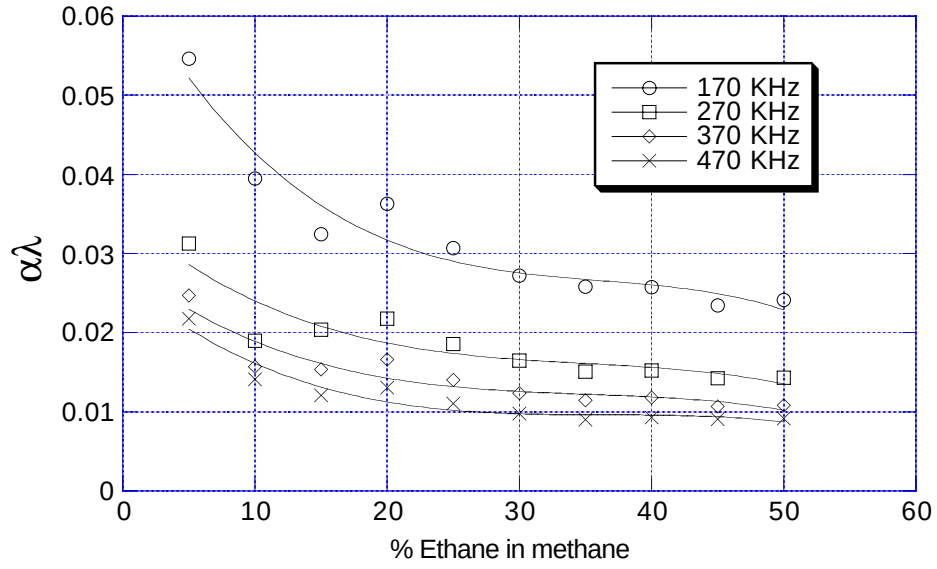

Figure 25. Attenuation per wavelength vs. ethane/methane concentration.

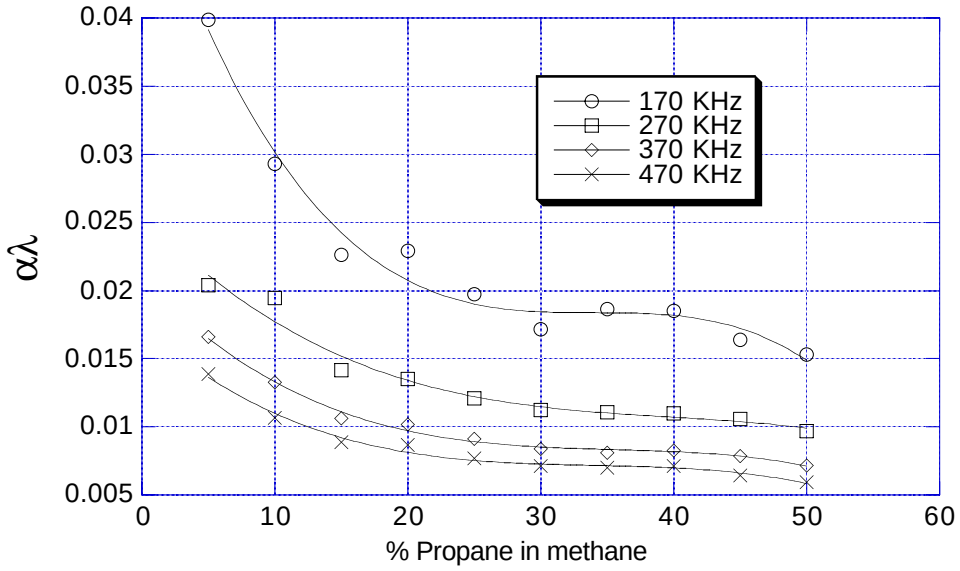

Figure 26. Attenuation per wavelength vs. propane/methane concentration.

4.0 CONCLUSIONS

We have completed the laboratory development of two sensors: the IMS NO_x sensor and the acoustic natural-gas sensor. Both sensors have been tested for their detection capabilities. The IMS sensor, using a spark-discharge ionization source, enables detection of NO_x based on changes in the IMS peak amplitude. The sensor responds to NO_x in various carrier gases and exhibits a sensitivity of ≈5 ppm and a linear dependence of up to 200 ppm. The moisture effect and methods to reduce it were examined and discussed. Design of a field sensor was also suggested.

The acoustic natural-gas sensor is a low-cost and robust sensor for inline application. We have demonstrated that the sensor can detect changes in binary-gas composition by measuring changes in either the SoS or acoustic attenuation. By combining the two measurements, one can determine the composition of a natural gas that contains multiple components. However, further development is needed to determine the sensitivity and reproducibility. At present, we believe the sensor can determine the percent of ethane or nitrogen in methane, but the percent of propane in methane may be difficult to determine.

REFERENCES

1. M. Benammar, “Techniques for measurement of oxygen and air-to-fuel ratio using zirconia sensors: A review,” Meas. Sci. Technol. 5, pp. 757-767, 1994.

2. D. J. Smith, J. F. Vetelino, R. S. Falconer and E. L. Wittman, “Stability, sensitivity and selectivity of tungsten trioxide films for sensing applications,” Sensors and Actuators B 13-14, pp. 264-268, 1993.

3. I. Sayago, et al., “Detection of toxic gases by a tin oxide multisensor,” IEEE Sensor J. 2, (5), pp. 387-393, 2002.

4. A. Oda, N. Imanaka and G-y Adachi, “New type of nitrogen oxide sensor with multivalent cation- and anion-conducting solid electrolytes,” Sensors and Actuators B 93, pp. 229-232, 2003.

5. L. Chen and S. C. Tsang, “Ag-doped WO_3-based powder sensor for the detection of NO gas in air,” Sensors and Actuators B 89, pp. 68-75, 2003.

6. T. Becker, S. Muhlberger, C. B. Braunmuhl, G. Muller and T. Ziemann, “Air pollution monitoring using tin-oxide-based microreactor systems,” Sensors and Actuators B 69, pp. 108-119, 2000.

7. M. Fleischer, M. Seth, C. D. Kohl and H. Meixner, “A study of surface modification at semiconducting Ga_2O_3 thin film sensors for enhancement of sensitivity and selectivity,” Sensors and Actuators B 35-36, pp. 290-296, 1996.

8. S. Chakane, A. Gokarna, and S. V. Bhoraskar, “Metallophthalocyanine-coated porous silicon gas sensor selective to NO_2,” Sensors and Actuators B 92, pp. 1-5, 2003.

9. J. Zhao, A. Buldum, J. Han and J. P. Lu, “Gas molecule adsorption in carbon nanotubes and nanotube bundles,” Nanotechnol. 13, pp. 195-200, 2002.

10. G. Lu, N. Miura and N. Yamazoe, “High-temperature sensors for NO and NO_2 based on stabilized zirconia and spinel-type oxide electrodes,” J. Mater. Chem. 7(8), pp. 1445-1449, 1997.

11. E. A. Mason, “Ion mobility: Its role in plasma chromatography,” *Plasma Chromatography*, Chapter 2, Plenum Press, New York, 1984.

12. G. A. Eiceman and Z. Karpas, *Ion mobility spectrometry*, CRC Press, 1994.

13. J. A. Jendrzejczyk, S. L. Dieckman, S. Slaughter and A. C. Raptis, “Response of a prototype vehicle exhaust gas sensor to various hydrocarbons and other constituents,” Argonne National Laboratory report, ANL-99/5, 1999.

14. J. A. Jendrzejczyk, S. L. Dieckman, S. Slaughter and A. C. Raptis, “Response of a prototype vehicle exhaust gas NO_x sensor to various hydrocarbons and other constituents,” Argonne National Laboratory report, ANL-99/19, 1999.

15. S. H. Sheen, H. T. Chien and A. C. Raptis, “ Advanced sensors for real-time control of advanced natural gas reciprocating engine combustion,” Argonne National Laboratory report, ANL-01/29, 2001.

16. M. A. Biondi and L. M. Chanin, “Blanc’s law – ion mobilities in helium-neon mixtures,” Phys. Rev. 122, pp. 843-847, 1961.

17. M. Tabrizchi, T. Khayamian and N. Taj, “Design and operation of a corona discharge ionization source for ion mobility spectrometry,” Rev. Sci. Inst. 71 (6), pp. 2321-2328, 2000.

18. C. A. Hill and C. L. P. Thomas, “A pulsed corona discharge switchable high resolution ion mobility spectrometer-mass spectrometer,” Analyst 128, pp. 55-60, 2003.

19. B. M. Penetrante, W. J. Pitz, M. C. Hsiao, B. T. Merritt and G. E. Vogtlin,” Effect of hydrocarbons on plasma treatment of NOx,” Proceedings of the 1997 Diesel Engine Emissions Research Workshop, San Diego, CA., July 28-31, 1997, pp. 123-128.

20. S. G. Ejakov, H.-T. Chien, R. Dorai, J. A. Jendrzejczyk, A. C. Raptis, S.-H. Sheen and J. H. Visser, “Modeling the use of a plasma source in ion mobility spectrometry for No_x detection in automotive exhaust,” ISIMS – 2001.

21. S. C. Bell and G. A. Eiceman, “Hand-held gas chromatography-ion mobility spectrometry for on-site analysis of complex organic mixtures in air or vapors over waste sites,” Los Alamos National Laboratory report LA-UR-91-434, 1991.

22. B. M. Smirnov, *Negative Ions*, p. 18, McGraw-Hill Inc., 1982.

23. M. F. Appel, W. E. vander Veer and T. Benter, “Conductive carbon-filled polymeric electrodes: novel ion optical elements for time-of-flight mass spectrometers,” J. Am. Soc. Mass Spectrom. 13, pp. 1170-1175, 2002.

24. G. Sberveglieri, editor, *Gas Sensors*, Kluwer Academic Publishers, 1992.

25. L. Zipser, F. Wachter and H. Franke, “Acoustic gas sensors using airborne sound properties,” Sensors and Actuators B 68, pp. 162-167, 2000.

26. M. O’Donnell, E. T. Jaynes and J. G. Miller, “General relationships between ultrasonic attenuation and dispersion,” J. Acoust. Soc. Am. 63(6), p. 1935, 1978.

27. A. B. Bhatia, *Ultrasonic Absorption*, p. 15, Oxford University Press, 1967.

28. K. F. Herzfeld and T. A. Litovitz, *Absorption and Dispersion of Ultrasonic Waves*, Academic press, New York, 1959.

29. H. J. Bauer, ”Phenomenological theory of the relaxation phenomena in gases,” Physical Acoustics Vol. II part A, pp. 48-132, 1965.

30. H. O. Kneser, ”Phenomenological theory of the relaxation phenomena in gases,” Physical Acoustics Vol. II part A, pp. 133-202, 1965.

31. D. Sette, A. Busala and J. C. Hubbard, “Energy transfer by collisions in vapors of chlorinated methanes,” J. Chem. Phys. 23, pp. 787-793, 1955.

32. Y. Dain and R. M. Lueptow, “Acoustic attenuation in three-component-gas-mixtures: Theory,” J. Acoust. Soc. Am. 109 (5), pp. 1955-1964, 2001.

33. Y. Dain and R. M. Lueptow, “Acoustic attenuation in three-component-gas-mixtures-: Results, J. Acoust. Soc. Am. 110 (6), pp. 2974-2979, 2001.

34. S. G. Ejakov, S. Phillips, Y. Dain, R. M. Lueptow and J. H. Visser, “Acoustic attenuation in gas mixtures with nitrogen: Experimental data and calculations,” J. Acoust. Soc. Am. 113 (4), pp. 1871-1879, 2003.

35. S. H. Sheen, H. T. Chien, and A. C. Raptis, “Ultrasonic techniques for detecting helium leaks,” Sensors and Actuators B 71, pp. 197-202, 2000.

Distribution for ANL-03-26

Internal

J. L. Carlson (2)	L. Johnson	W. Schertz
H. T. Chien (10)	J. Harmon	S.-H. Sheen (15)
H. Drucker	R. B. Poeppel	TIS files
N. Gopalsami	A. C. Raptis	

External

ANL-E Library
ANL-W Library
U.S. Department of Energy
    Office of Distributed Energy Resources
        Patricia Hoffman
    Golden Field Office
        Paul Bakke
    Office of Power Technology
        J. A. Mavec
        J. M. Livengood
Caterpiller, Inc.
    G. Gerber
Cummins Engine Company, Inc.
    Axel Zur Loye
Waukesha Dresser
    Jim Drees
Energy Technology Division Review Committee
    H. K. Birnbaum, University of Illinois at Urbana-Champaign
    I.-W. Chen, University of Pennsylvania
    F. P. Ford, Rexford, NY
    S. L. Rhode, University of Nebraska-Lincoln
    H. S. Rosenbaum, Fremont, CA
    S. L. Sass, Cornell University
    R. Zoughi, University of Missouri-Rolla